ORIGINAL RESEARCH ARTICLE

Archeometallurgical Investigation of a Fragment from a Medieval Sword Blade

Paolomarco Merico[1] · Michela Faccoli[1] · Roberto Gotti[2] · Giovanna Cornacchia[1]

Abstract

A fragment from a medieval sword blade was investigated by metallography, Vickers microhardness tests and slag inclusions analysis are to extract technological information about its manufacturing process. Optical microscopy observations and microhardness measurements indicated that the sword blade was forged *via* hammer welding, combining different steel bars for an optimal balance of hardness and toughness. A steeling technique involved wrapping a steel bar around a composite billet, crafted by enclosing a hypoeutectoid steel bar around a near-eutectoid steel core. Moreover, it was found that the hardness of the cutting edges was increased with a quenching heat treatment. After quenching, the blade exhibited martensitic microstructure with Vickers microhardness ranging from 500 to 640 $HV_{0.3}$. The compositional data of a large set of nonmetallic inclusions were collected by scanning electron microscopy coupled with X-ray dispersive spectroscopy. Slag inclusion analysis and multivariate statistics confirmed the blade's composite nature and revealed distinct smelting and forging-related SI groups. Liquidus temperatures indicated smelting temperatures of at least 1156°C for the external section and 1031°C for the internal. The forging temperature was estimated at a minimum of 1143°C. These findings provide insight into the blade's metallurgical history.

Keywords Archeometallurgy · Sword · Middle ages · Scanning electron microscopy · Inclusion analysis

Introduction

Medieval swords, intertwining functionality with aesthetic-symbolic power, stand as one of the most advanced expressions of medieval metallurgical craftsmanship. In this light, they potentially contain key technological information that is crucial in advancing the knowledge of the history of European ironmaking and forging processes. It is worth noting that high-quality swords needed to exhibit essential mechanical properties such as high yield strength and fracture toughness as well as valuable aesthetic features [1, 2]. To fulfil these requirements, it was important to use suitable iron and steel in terms of homogeneity and cleanliness, along with proper forging strategies. During the Middle Ages, the European production of wrought iron and steel

required for sword making encompassed the utilization of both direct and indirect ironmaking methods [3]. Specifically, the direct method involved the solid-state reduction of iron ore (typically a mixture of iron-rich minerals and nonmetallic siliceous gangue) fed with charcoal and fluxes into the "bloomery" furnace. In particular, charcoal combustion generated a reducing environment highly enriched in carbon monoxide gas. The interaction between reducing gas and the iron ore promoted the formation of metallic iron particles. Moreover, a fluid iron silicate slag was generated at a temperature of ~1200°C by the chemical reaction between iron oxides and gangue compounds. Metallic iron particles embedded within the slag were protected from re-oxidation and sintered together at the bottom of the furnace into a sponge-like iron mass referred to as "bloom." After smelting, the bloom was homogenized and partially purified from slag through hot hammering and multi-folding [3]. From the Late Middle Ages onward, the introduction of the indirect method allowed the mass production of wrought iron and steel by decarburization of cast iron produced in a shaft furnace. This process consists of the oxidation of cast iron fragments blended with charcoal and fluxes in an

✉ Michela Faccoli
  michela.faccoli@unibs.it

1 Department of Mechanical and Industrial Engineering, University of Brescia, Via Branze 38, 25123 Brescia, Italy

2 The Martial Arts Museum, via Garibaldi 3, 25082 Botticino, BS, Italy

open hearth [4]. In the past years, many studies based on destructive (e.g., metallographic analysis) and noninvasive analysis (e.g., X-ray computer tomography) have been conducted to reconstruct the manufacturing techniques of medieval swords [5–7]. Based on these research works, the most advanced method for the fabrication of early medieval swords (*namely*, double-edged spathae) integrates both "pattern welding" and "steeling" techniques. In particular, pattern-welded sword blades were skillfully crafted by assembling in various arrangements multiple folded or twisted steel bars with different phosphorous and carbon content [8, 9]. Subsequently, post-forging grinding and etching of the blade surface revealed wonderful ornamental decorations arising from the complex welding patterns [10, 11]. On the other hand, the steeling technique was employed to equip the pattern-welded blade with two steel cutting edges that could be hardened by quenching heat treatment [12]. In the Late Middle Ages, the adoption of the pattern-welding technology declined almost entirely and sword blades were mainly realized in a less elaborate and aesthetic-focused fashion [13]. In particular, sword blades could be produced from a single piece of steel or by combining iron and steel bars following different assembling strategies. This could be achieved by joining steel edges to an iron body, inserting a steel bar between two layers of iron, or wrapping a layer of steel around an iron core. It should be emphasized that the execution of all these techniques required the ability to master the solid-state joining of iron and steel by hammer welding. In particular, the metal pieces to be joined were heated up to an approximate temperature of °C. Their surfaces were coated with silica-rich smithing flux which reacting with the iron oxide scale formed a fluid fayalite slag. This slag could be easily expelled under the hammer blows pressure facilitating intimate contact between the two surfaces and enabling their welding by an interatomic diffusion mechanism [12, 14, 15]. In this context, the objective of this research was to examine a fragment from a medieval sword blade donated from a private collection with the aim to provide a comprehensive reconstruction of the smelting and forging processes involved in its production. To achieve these objectives, a state-of-the-art methodology based on metallography and slag inclusions (SI) analysis was adopted [16–25].

Materials and Methods

The Sword Blade Fragment: Preliminary Description and Macro-observation

Visual examination revealed that the blade fragment was highly affected by corrosion phenomena and featured a deteriorated surface (Fig. 1a). The fragment belonged to a tapered double-edged sword with a lenticular cross section. In addition, the terminal portion of a narrow tapered fuller runs in the middle of the blade fragment (Fig. 1a). The main sword measurements are as follows: total length = 270 mm, maximum width = 46 mm, and minimum blade width = 39 mm. The blade and fuller morphology suggest that the blade fragment likely belonged to a medieval sword, possibly of type XII in the typological classification framework designed by Oakeshott [1, 26]. However, caution should be exercised regarding the proposed hypothesis about the exact sword type due to the impossibility to collect dimensional data of the whole blade and other sword components such as pommel, cross, and tang. It is worth noting that the fullers present in swords of type XII generally extend longitudinally for approximately three-quarters of the total

Fig. 1 (a) Photographic image of the blade fragment and (b) sampling scheme; the analyzed sections (S1, S2, and S3) belong to the samples highlighted with striped backgrounds
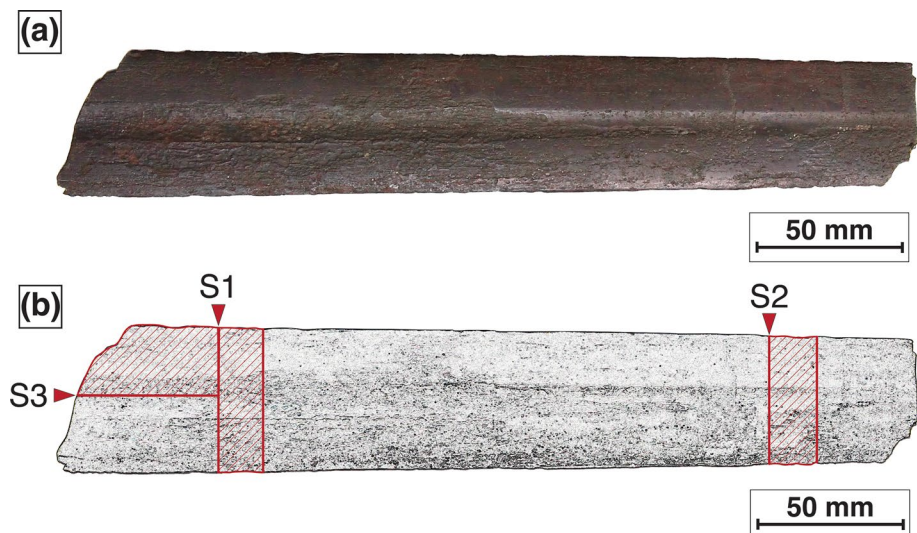
blade length. Based on this premise, it can be deduced that the sword fragment should be probably positioned within the initial three-quarters of the blade length. Two cross-sectional segments (S1, S2) along with a longitudinal section (S3) were extracted from the sword blade fragment for analysis. The sampling methodology is illustrated in Fig. 1b.

Experimental Methods

The samples were extracted from the sword fragment using a Struers cutoff machine and cooled with cutting fluid to ensure that the original steel microstructure remained unaltered during the sampling process. Each blade section was prepared following a standard metallographic procedure by grinding with silicon carbide abrasive papers (grades ranging from 80 to 1200) and polishing with polycrystalline diamond pastes (3 μm and 1 μm). The morphology and spatial distribution of micron-sized slag inclusions (SI) entrapped within the metal matrix were observed *utilizing* light optical microscopy (LOM) on the as-polished sections using a LEICA DMI 5000 M optical microscope.

Subsequently, all specimens were etched by immersion in 1 pct Nital solution (1 vol pct HNO_3 in ethanol) to investigate the nature and distribution pattern of the steel microstructural constituents. This methodology permits a detailed characterization of the microstructural features that are essential for the reconstruction of the manufacturing process of ferrous composite artifacts [16, 17, 19–21]. As an illustrative instance, welding lines are typically demarcated by microstructural discontinuities and SI alignments. Vickers microhardness measurements were taken using a Mitutoyo HM-200 tester, under a 300-g load applied for 15 seconds on the polished and etched samples to check the identification of each microstructural constituent. Subsequently, the chemical composition of 66 SI on repolished transverse S2 section and longitudinal S3 section was semiquantitatively measured by X-ray energy-dispersive spectroscopy (EDS) coupled with LEO EVO-40 XVP Scanning Electron Microscope (SEM). The analyses were performed by examining all SI surfaces through area acquisition. The chemical data are given in terms of the following stoichiometric oxides: Na_2O, MgO, Al_2O_3, SiO_2, K_2O, CaO, TiO_2, MnO, FeO, SO_2, and P_2O_5. The mineralogy of slag inclusions was investigated by SEM in backscattering mode (BSD). Moreover, the area of each SI was measured with the software ImageJ [27].

Slag Inclusions Classification and Data Treatment

Medieval ferrous alloys are generally characterized by a significant amount of SI [28]. In particular, SI can remain embedded in the metallic matrix during both smelting and forging processes. The entrapment of slag inclusions (SI) associated with the smelting process was facilitated by the

partially solid-state characteristics inherent to iron production techniques during the Middle Ages, encompassing both direct processes such as iron ore reduction within the bloomery furnace, and indirect processes like the refinement of cast iron. This technological feature prevented an effective separation between the liquid metallurgical slag and the solid ferrous alloy. On the other hand, SI can also be derived from the forging process. In fact, joining operations *via* hammer welding required necessitated the application of a sand flux onto the metal surfaces The chemical interaction between the silica-rich smithing flux and the iron oxide scale promotes the formation of fayalitic slag whose remnants can eventually remain entrapped at welding interfaces as forging SI. It is important to note that SI potentially retain a chemical signature linked to specific smelting and forging systems (mainly defined by the chemical features of iron ore, lining, charcoal, and fluxes) [29]. In addition, smelting and forging-derived SI can contain thermo-chemical information about the reduction and smithing processes, respectively [18]. Therefore, it is essential to determine the formation origin of each analyzed SI. For this purpose, two complementary SI classification strategies introduced by Dillmann and L'Héritier [22] and Charlton et al. [30] were employed in this research work. Following these approaches, SI can be described as multicomponent oxide systems constituted by two main types of oxides: reduced compounds (RCs) and nonreduced compounds (NRCs). Notably, only NRCs (*e.g.*, Al_2O_3, K_2O, MgO, CaO) carry useful information to select SI families linked to different smelting and forging systems. Conversely, the amounts of RCs (e.g., FeO, P_2O_5) are strongly influenced by the variation of redox conditions (i.e., oxygen chemical potential and temperature) even within the same technological system. Therefore, RCs can be heterogeneously scattered inside SI groups with the same origin. Conversely, the homogeneity of NRCs ratios is assumed by Dillmann and L'Héritier [22] as a key criterion to recognize smelting-related SI with a similar genesis. In addition, forging SI can be marked by more variable NRCs ratios and higher SiO_2–Al_2O_3 ratios than smelting-derived SI if silica-rich smithing flux was used. Moreover, Charlton's method employs multivariate statistical analysis techniques, i.e., principal component analysis (PCA) coupled with hierarchical cluster analysis (HCA). The elemental chemical data acquired by SEM/EDS were converted to oxides weight percentages (wt.%) by stoichiometry. In addition, PCA was performed on log-ratio transformed compositional data to equalize both the magnitude and variance of NRCs [31]. Only well-quantified NRCs were considered: Al_2O_3, SiO_2, CaO, and MnO. The data pre-processing transformation is expressed by Formula (1):

$$Xi_{NRC} = \log(Ei_{NRC}) - g(\log E_{NRC}) \tag{1}$$

where Xi_{NRC} is the ith transformed value for each NRC (i.e., Al_2O_3, SiO_2, CaO, MnO), Ei_{NRC} is the amount of the ith NRC, and $g(\log E_{NRC})$ is the geometrical mean of the logged NRCs.

To distinguish the main SI clusters, HCA based on the Ward method with Euclidean distance was adopted. The data treatment was performed using R 3.6.1, Excel, and OriginLab software environment for statistical computing and graphics [32].

Results and Discussion

Metallographic Examination and Microhardness Measurements

Three sections (Fig. 1b) sampled near the lower (S1, S3) and upper (S2) ends of the sword blade fragment were investigated by light optical microscopy. The examination of the sections in as-polished condition revealed the presence of multiple SI bands oriented along the main hot plastic deformation directions (Figs. 2, 3, and 4). The continuity of the SI stringers near the outer surface of the blade fuller in the S1 and S2 sections indicates that it was shaped by hot plastic deformation (Figs. 2b and 3b). Corrosion-induced cracks

Fig. 2 (a) As-polished transverse section S1 (collage of micrographs with 50X magnification), (b) continuous SI lines near the outer surface of the fuller, and (c) crack due to corrosion
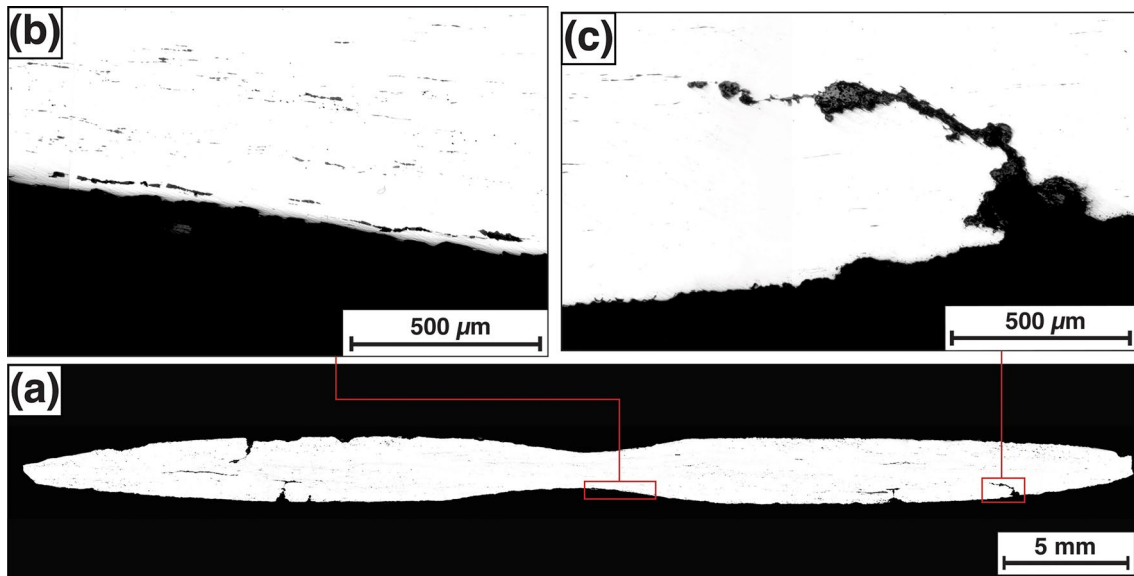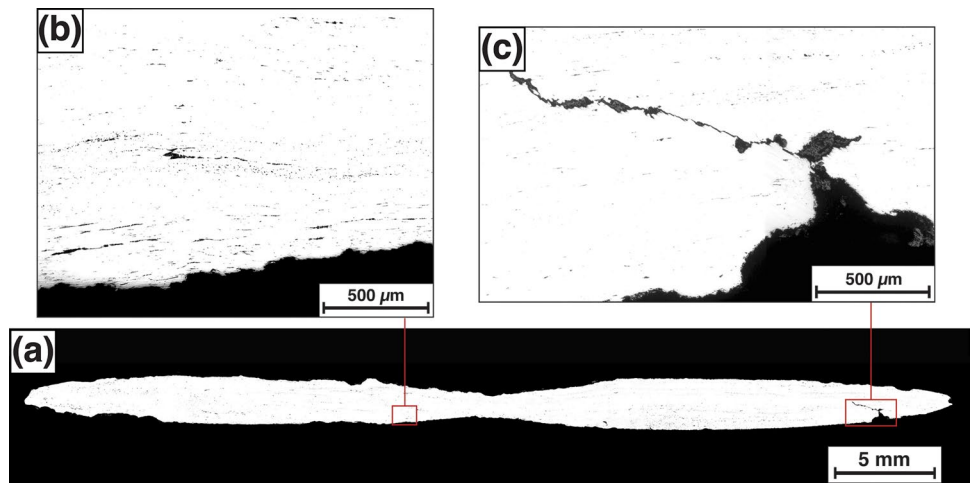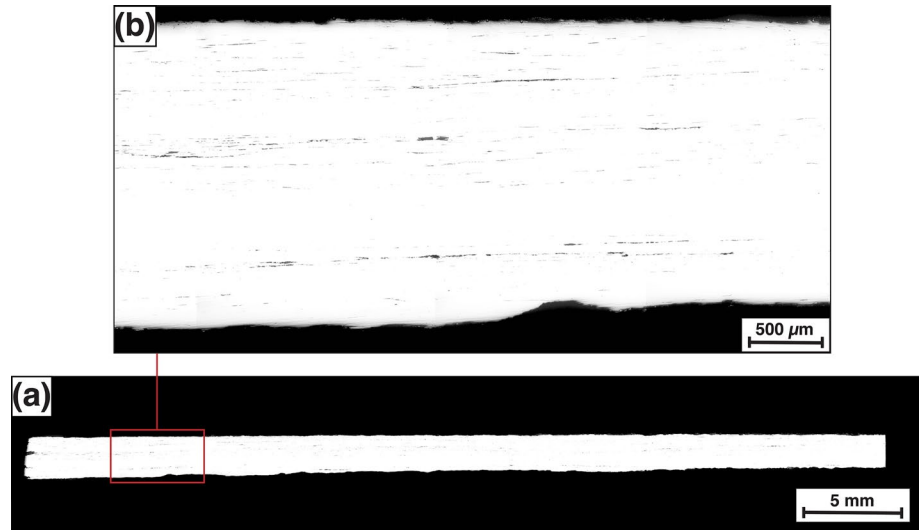

Fig. 3 (a) As-polished transverse section S2 (collage of micrographs with 50X magnification), (b) continuous SI lines near the outer surface of the fuller, and (c) crack due to corrosion

Fig. 4 (**a**) As-polished longitudinal section S3 (collage of micrographs with 50X magnification) and (**b**) multiple SI stringers

partially filled with oxidation products were detected in S1 and S2 sections (Figs. 2c and 3c). Furthermore, a higher density of SI lines was observed near the inner and outer zones in the longitudinal section S3 (Fig. 4b).

Each section was analyzed *via* optical microscopy after 1 pct Nital etching. The position of the identified microstructural constituents in the S1 section is shown in Fig. 5a. Most of the section outer zone, encompassing the left and
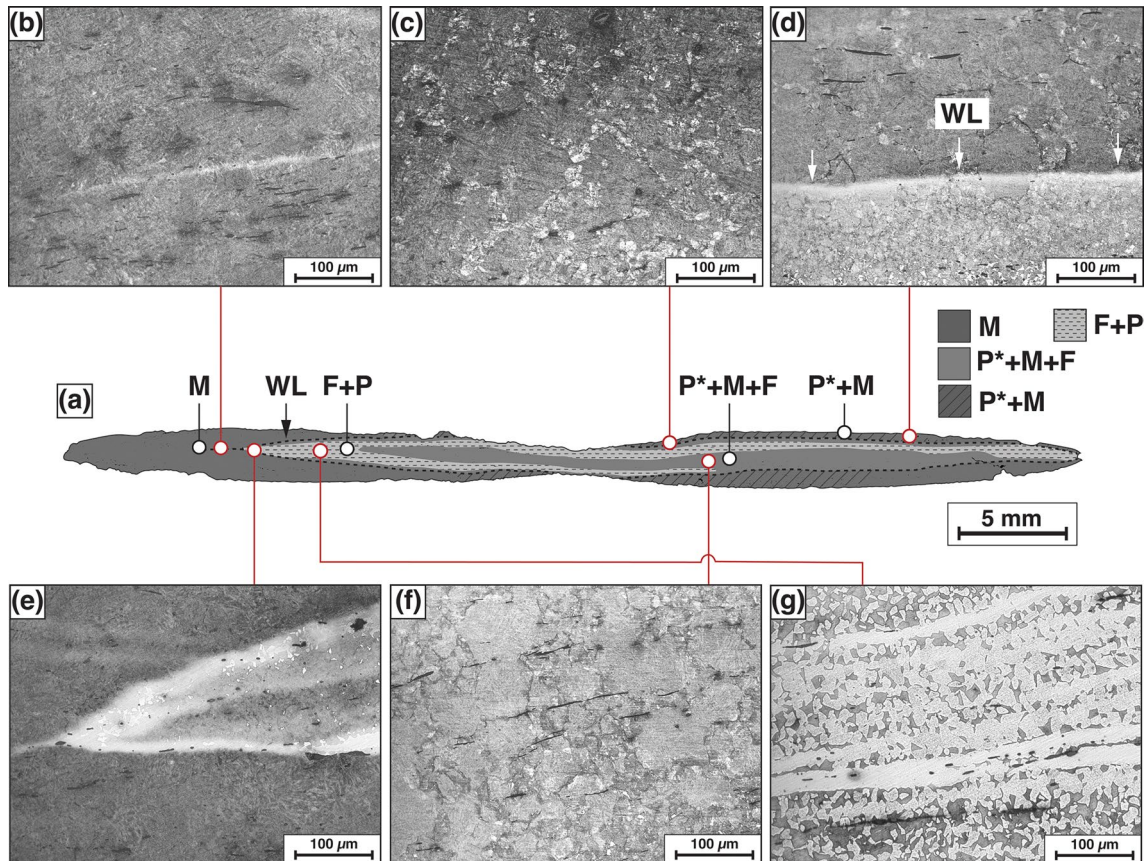

Fig. 5 (**a**) Distribution map of the main microstructural constituents and features observed in the S1 section and (**b-g**) some representative 200X magnification optical micrographs (F = ferrite, P = pearlite, P* = nodular pearlitic colonies, M = martensite, WL = white line)

partially the right cutting edge, exhibits a martensitic microstructure (M) (Fig. 5b, high-magnification image in Fig. 6) often accompanied by pearlitic nodules (P* + M) localized at prior austenitic grains boundaries in certain regions (Fig. 5c, high-magnification image in Fig. 7). The complete transitional region demarcating the outer and inner segments of the section is seamlessly marked by a sharp "white line" (WL), indicative of a light-etched band (Fig. 5d and e). It is of noteworthy significance that this attribute can be reliably recognized as a distinctive indicator for the discernment of hammer-welding interfaces [33, 34]. In fact, due to the smithing oxidizing environment, an oxide scale layer (termed "hammer scale") was usually formed on the surface of the ferrous lumps to be joined by hammer welding. If iron and steel contained alloying elements that oxidize less rapidly than iron (e.g., phosphorus and arsenic), then the sub-scale metal matrix becomes selectively enriched with these alloying elements. Moreover, this phenomenon promotes a local increase in etching resistance which can explain the presence of light-etching bands at the hammer-welding joint interface. On the other hand, the inner part of section S1 featured a banded-like microstructure. Specifically, the central portion is marked by traces of allotriomorphic ferrite and nodular pearlitic colonies at the prior austenitic grain boundaries embedded within a martensitic matrix (P* + M + F) (Fig. 5f, high-magnification image in Fig. 8). In addition, a significant portion of this region is surrounded by two ferritic–pearlitic (F + P) layers which exhibit a stratified and distinctive layered structure, attributed to the presence of well-defined white lines (WL) (Fig. 5g). This feature is compatible with the execution of multiple folding and hammer-welding cycles. Moreover, an asymmetry in the distribution of microstructural constituents was noted within both the outer and inner segments of the cross section
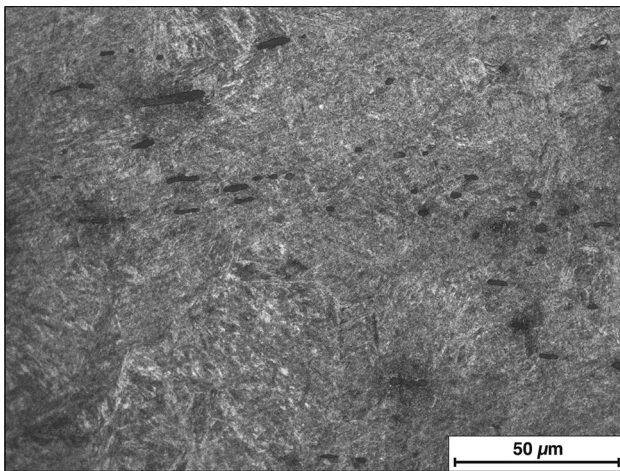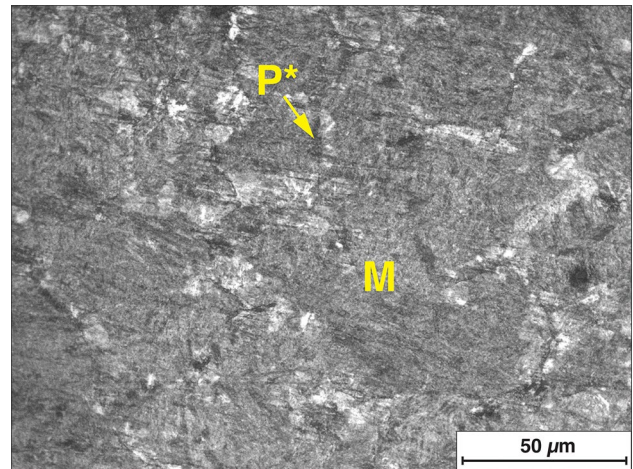

Fig. 7 Nodular pearlitic colonies in a martensitic matrix (500X magnification, P* = nodular pearlitic colonies, M = martensite)

(Fig. 5a). The presence of this characteristic is plausible due to the V-shaped joining of distinct steel bars.

Similar results were obtained by investigating the etched S2 transverse section. The distribution of the microstructural constituents is shown in Fig. 9a. In the outer region, a fully martensitic microstructure (M) was observed (Fig. 9b). The inner zone is constituted by three layers. The core featured traces of allotriomorphic ferritic and nodular pearlitic colonies at the prior austenitic grains boundary in a martensitic matrix (P* + M + F) (Fig. 9c). This core is wrapped externally by two layers which are characterized by a ferritic–pearlitic (F + P) microstructure (Fig. 9d). As noted in the S1 section, a white line (WL) sharply demarcates the
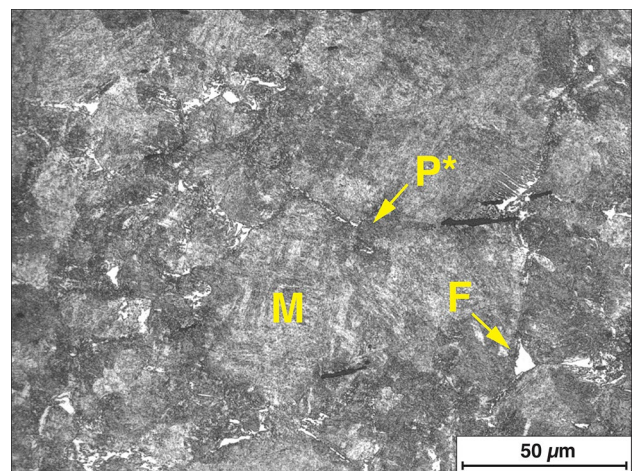

Fig. 6 Martensitic microstructure (500X magnification)

Fig. 8 Nodular pearlitic colonies and traces of allotriomorphic ferrite in a martensitic matrix (500X magnification, F = ferrite, P* = nodular pearlitic colonies, M = martensite).
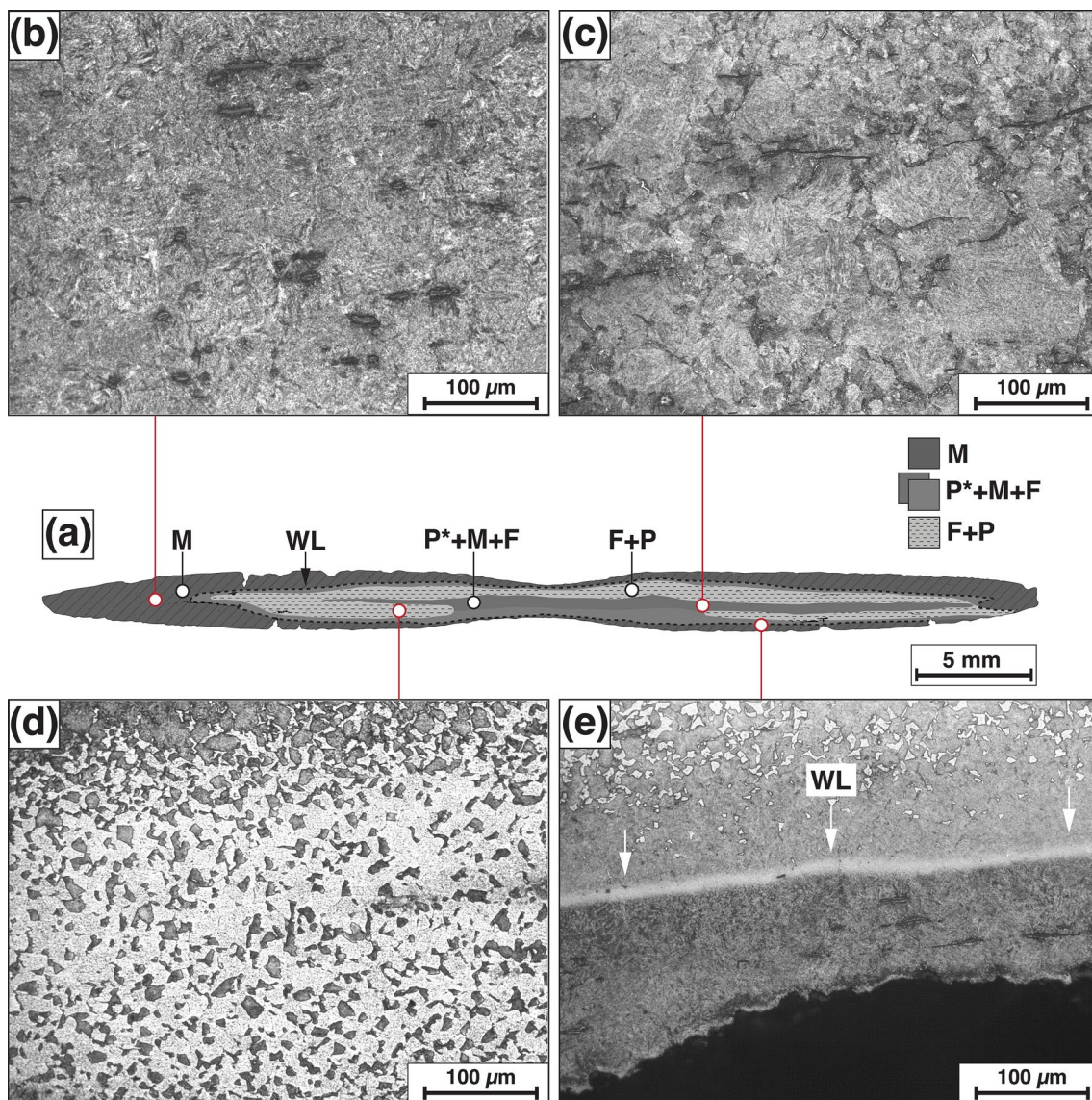
Fig. 9 (**a**) Distribution map of the main microstructural constituents and features observed in the S2 section and (**b-e**) some representative 200X magnification optical micrographs (F = ferrite, P = pearlite, P* = nodular pearlitic colonies, M = martensite, WL = white line)

boundary between the martensitic and ferritic–pearlitic regions (Fig. 9e).

The microstructure observed in the longitudinal section S3 is compatible with the results reported for the transverse sections S1 and S2 (Fig. 10a). The section is marked by a multi-layer appearance (Fig. 10b). In particular, a fully martensitic microstructure (M) was detected in the two external layers (Fig. 10c). The inner portion of the section is constituted by a core interposed between two other layers. The core is marked by nodular pearlitic colonies and ferritic traces in a martensitic matrix (P* + M + F) (Fig. 10d). Conversely, the two enveloping layers exhibit bands of ferritic–pearlitic composition (F + P) (Fig. 10e). Moreover, SI stringers were identified within the ferritic bands (Fig. 10e).

This aspect reinforces the hypothesis that multiple folding and forge welding cycles were performed. The demarcation interface between the ferritic–pearlitic domains and the outer martensitic regions is distinctly marked by white lines (WL) and SI alignments (Fig. 10f).

Concerning the hardness analysis, Vickers microhardness measurements were taken for all three sections. The distribution map of microhardness indentations and measurement data for section S1 is shown in Fig. 11a and b-c, respectively. Further information regarding the other investigated sections and a comprehensive summary of the microhardness measurements can be found in Supplementary Electronic Material, specifically in Figures S-1 and S-2, and Table S-I. Considering all the results achieved, the microhardness
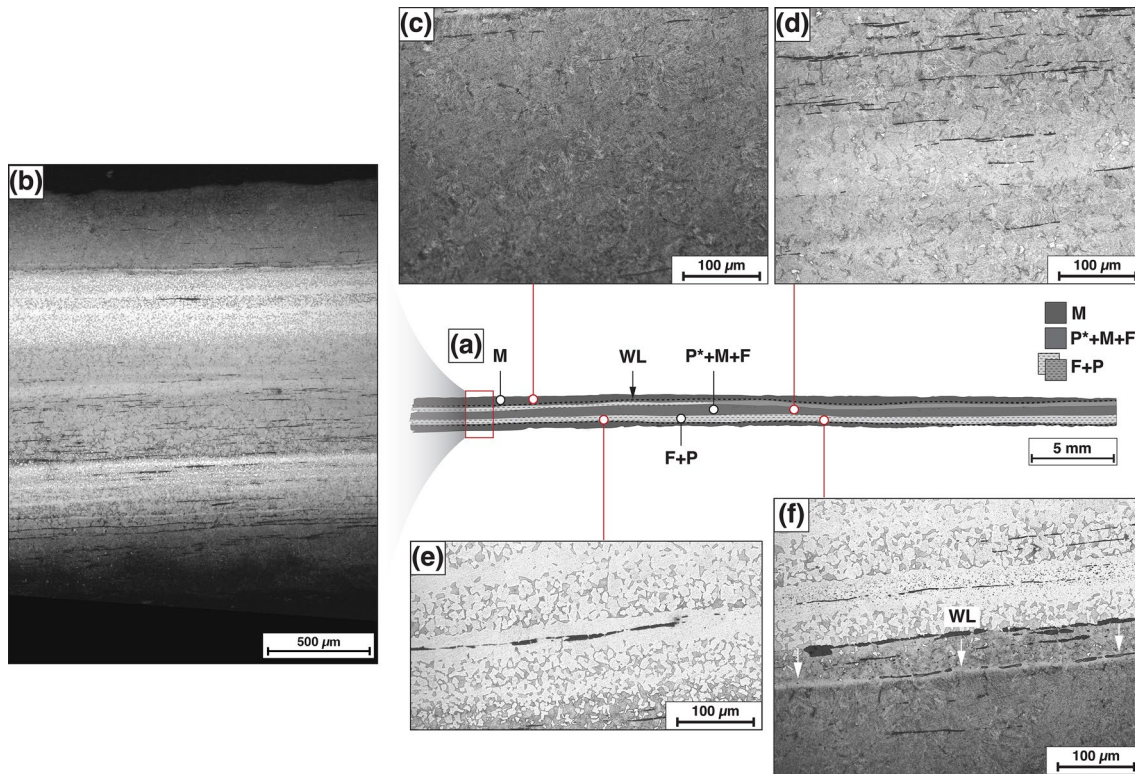
Fig. 10 (**a**) Distribution map of the main microstructural constituents and features observed in the S3 section, (**b**) detail of the layered microstructure (collage of micrographs with 50X magnification), and (**c-f**) some representative 200X magnification optical micrographs (F = ferrite, P = pearlite, P* = nodular pearlitic colonies, M = martensite, WL = white line)

Fig. 11 (**a**) Distribution map of Vickers microhardness indentations on S1 section and resulting measurements along (**b**) horizontal (L1) and (**c**) vertical (L2-L6) lines (F = ferrite, P = perlite, P* = nodular pearlitic colonies, M = martensite)
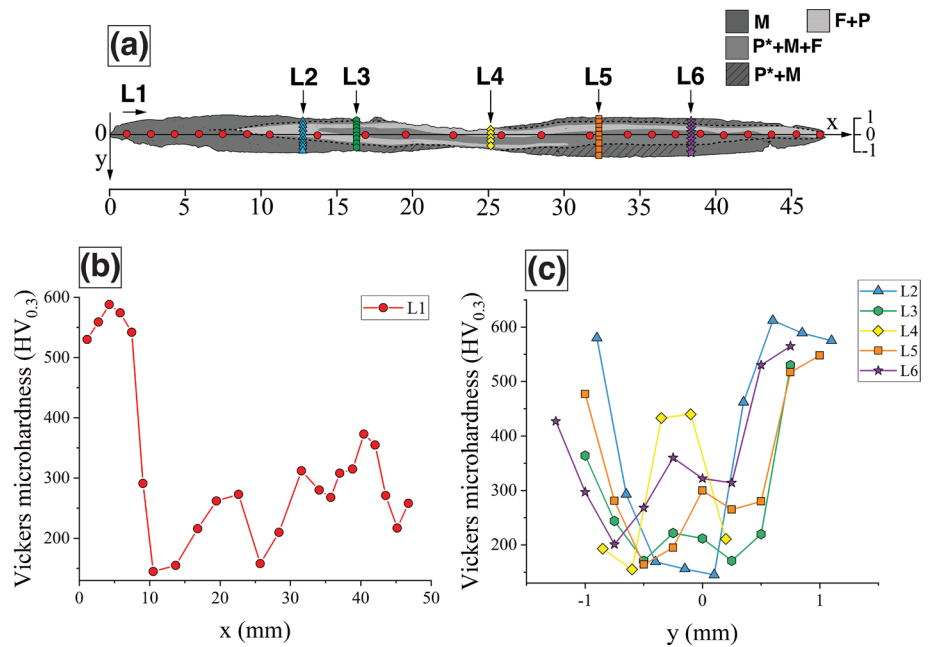
values in the ferritic–pearlitic (F + P) zones vary in the range of 145 to 293 $HV_{0.3}$. The zones marked by a martensitic microstructure with nodules of pearlite (P* + M) feature a

microhardness in the range of 427 to 477 $HV_{0.3}$, whereas the microhardness values decrease in the range 292 to 420 $HV_{0.3}$ where ferrite is also present (P* + M + F). Additionally, in

the fully martensitic (M) zones the microhardness measurements vary between 500 and 640 $HV_{0.3}$.

The comprehensive analysis of the metallographic characteristics and Vickers microhardness data enables the reconstruction of the principal stages involved in the manufacturing process of the medieval sword blade to which the analyzed fragment belongs. The construction of the internal part of the blade seemingly followed a sequential approach: A hypoeutectoid steel bar was V-shaped, wrapped around, and forge-welded to a more carburized steel billet, which represents the blade core (Fig. 12a). It was noted that the hypoeutectoid steel bar exhibited a layered and stratified microstructure potentially arising from multiple and iterative sequences of folding and forge-welding cycles. Subsequently, a steel bar, corresponding to the blade cutting edges, underwent enwrapping and joined *via* hammer welding to the composite billet (Fig. 12b). The blade shaping and refinement were performed through hot plastic deformation by means of hammering processes. Moreover, the presence of martensite is congruous with a quenching heat treatment strategy involving rapid cooling, aimed at increasing the hardness of the blade cutting edges. It should be observed that in some regions and especially in the central core, the cooling rate was insufficient to achieve a fully martensitic microstructure. Overall, this manufacturing process was applied to achieve a good balance between the desired hardness of the cutting edges and the necessary resilience of the blade [6].

Slag Inclusions Classification

The chemical composition of 66 SI was obtained by SEM/EDS (Supplementary Table S-II). The main results of PCA coupled with HCA are illustrated in Fig. 13. In particular, SI were clustered into three groups within the PC space (Fig. 13a) by cutting the dendrogram plot at a height of 15 (Supplementary Figure S-3).

For each SI group, the area-weighted mean percentages of oxides were calculated using Formula (2):

$$\text{wt.\% Oxide}_j^* = \sum_{i=1}^{n_j} \text{wt.\% Oxide}_{ij} \times \frac{S_{ij}}{S_{Tj}} \qquad (2)$$

where wt.% Oxide_j^* represents the weighted average percentage of a specific oxide for the jth group, wt.% Oxide_{ij} denotes the oxide weight percentage for the ith SI in the jth cluster, S_{ij} corresponds to the ith SI surface in the jth group, while S_{Tj} is the total surface area of the jth group. The weighted average percentages of oxides for each SI group are listed in Table 1.

Group 1 (orange diamond symbols) is separated along the two variables SiO_2 and Al_2O_3 which are positively correlated as indicated by the small angle between their loading vectors in the PC1–PC2 plane (Fig. 13a). Indeed, group 1 exhibits higher amounts of SiO_2 and Al_2O_3 and a lower amount of MnO compared to groups 2 and 3 (Table 1). It is important to observe that group 1 encompasses all the SI located at white lines (star symbols). White lines represent the hammer-welding joining interface separating the external martensitic and internal ferritic–pearlitic zones of the blade (Fig. 13c and d). Hence, it is plausible to categorize these SI as forging-related, presumably formed through the chemical interaction between the iron oxide scale and smithing flux during the hammer welding joining process. This hypothesis prompts the question of whether all constituents within group 1 share a forging-related origin. To further explore the chemical variability of group 1, a subsequent PCA/HCA analysis was conducted, focusing selectively on SI of group 1. It was found that three subgroups of group 1 can be identified (Fig. 13b). Specifically, subgroup 1(1) (red circles) tends to separate along the single-variable MnO in the PC1–PC2 plane because the amount of MnO is greater compared to the other subgroups (Table 1). It is worth noting that MnO derives from manganiferous iron ore gangue. Therefore, subgroup 1(1) probably was generated during the smelting process. Subgroup 2(1) (yellow inverted triangles) is demarked by the positively correlated oxides SiO_2 and CaO (Fig. 13b). This feature can be explained by the contamination of SiO_2-rich SI with CaO-bearing ash. Notably, subgroup 2(1) encompasses three of the four SI located at
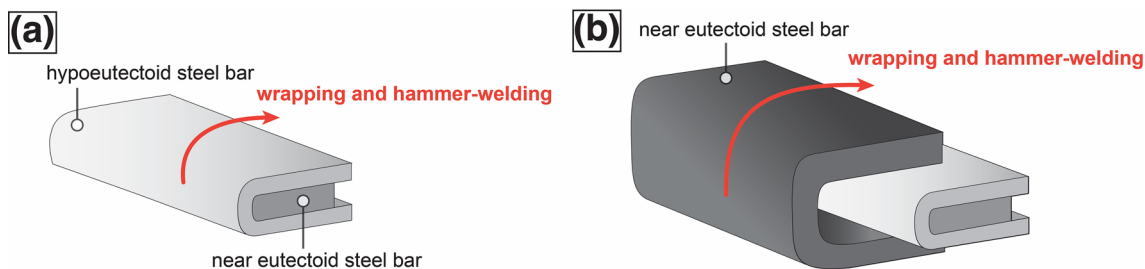

Fig. 12 Manufacturing process of the composite steel block: (**a**) production of the internal part of the blade and (**b**) steeling

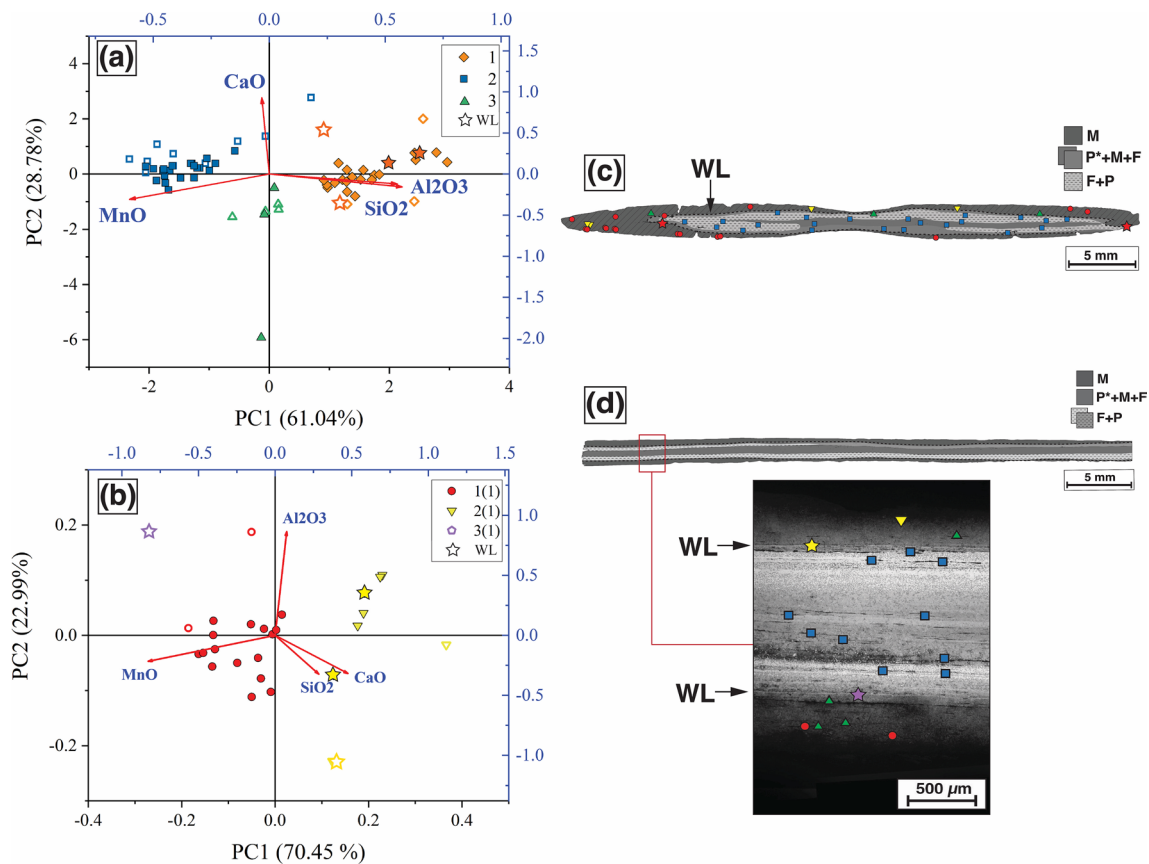**Fig. 13** (**a-b**) Projection of SI chemistry on PC1–PC2 plane (solid and open versions of the same symbol refer to transverse S2 and longitudinal S3 sections, respectively) with loading vectors plot (the percentage of variation explained by each PC is indicated in brackets) and position of SI groups on microstructural constituents maps of (**c**) section S2 and (**d**) section S3 (F = ferrite, P = pearlite, P* = nodular pearlitic colonies, M = martensite, WL = white line)

white lines (star symbols). Considering all these results, subgroup 2(1) can be classified as forging-related. Subgroup 3(1) (violet star symbol) includes only one SI located on a white line. Moreover, the chemical composition of this SI is dominated by FeO (Table 1). Consequently, it can be classified as a residue of the iron oxide scale that originated during the forging process. Group 2 (blue squares) is positioned at the upper extreme of the MnO loading vector which is anti-correlated to SiO_2 and Al_2O_3 in the PC1–PC2 plane (Fig. 13a). Indeed, group 2 is characterized by a higher concentration of MnO and a lower content of SiO_2 and Al_2O_3 compared to the other groups, as illustrated in Table 1. As previously noted, the significant amount of MnO serves as a definitive indicator that enables the classification of group 2 as smelting-related. Group 3 (green triangles) is located near the origin of the PC1–PC2 plane (Fig. 13a) and exhibits chemical features that are intermediate between groups 1 and 2 (Table 1). In addition, the high concentration of MnO points out that the genesis of group 3 is smelting-related.

To further the SI classification, FeO–SiO_2 (Fig. 14a) scatterplot was examined, along with three NRCs bivariate scatterplots: SiO_2–Al_2O_3 (Fig. 14b), MnO–SiO_2 (Fig. 14c), and CaO–SiO_2 (Fig. 14d). In accordance with the PCA/HCA results, the point clouds corresponding to group 1 (comprising subgroups 1(1), 2(1), and 3(1)) and group 2 display distinct linear trends due to the different NRCs ratios. According to Dillmann and L'Héritier [22], these results confirm that the genesis of groups 1 and 2 is different. In particular, group 1 exhibits higher SiO_2–Al_2O_3 and MnO–SiO_2 ratios than group 2, while the CaO–SiO_2 ratio is lower. Group 3 is characterized by similar SiO_2–Al_2O_3 and CaO–SiO_2 ratios with respect to group 1. However, the MnO–SiO_2 ratio of group 3 is intermediate between groups 1 and 2. Within group 1, subgroup 2(1) exhibits a lower MnO–SiO_2 ratio as expected in the case of low-MnO forging SI.

The positions of the SI groups on the microstructural constituents maps of sections S2 and S3 are shown in Fig. 13c and d. Notably, smelting-related groups 1(1) and 2 are located in the external and internal parts of the blade, respectively. On

Table 1 Average weighted oxides percentages (wt.%) for Each SI group and for subgroups of Group 1

Group	Na$_2$O (wt.%)	MgO (wt.%)	Al$_2$O$_3$ (wt.%)	SiO$_2$ (wt.%)	K$_2$O (wt.%)	CaO (wt.%)	TiO$_2$ (wt.%)	MnO (wt.%)	FeO (wt.%)	SO$_2$ (wt.%)	P$_2$O$_5$ (wt.%)
1	0.88	1.80	5.65	57.88	1.15	7.80	0.10	4.12	20.61	0.00	0.00
2	0.07	2.71	4.77	33.09	0.89	10.34	0.08	15.30	31.03	0.09	1.57
3	0.84	1.64	3.99	43.41	0.83	4.99	0.76	8.89	34.37	0.00	0.27
1(1)	0.97	2.18	6.03	63.56	1.28	8.17	0.17	5.34	12.30	0.00	0.00
2(1)	0.75	1.22	5.12	49.50	0.96	7.32	0.00	2.18	32.94	0.00	0.00
3(1)	0.00	0.00	0.85	3.82	0.00	0.66	0.00	0.71	93.96	0.00	0.00

the other hand, smelting-related group 3 and forging-related groups 2(1) and 3(1) are preferentially positioned near the interface between these two zones. This distribution pattern clearly reflects the composite nature of the blade. Consistent with the metallographic analysis results, the distinct chemical features of smelting-related groups 1(1) and 2 suggest that the outer and inner zones of the blade were manufactured at least with two steel bars produced in different technological systems. Furthermore, despite group 3 being located in the microstructurally heterogeneous inner part of the blade, the chemical composition of its SI is relatively homogeneous. This observation supports the hypothesis that the inner portion of the blade consists of a composite billet manufactured combining low- and high-carbon steels with a similar origin. A mineralogical investigation was carried out by SEM/EDS analysis to extend the SI characterization. Two main SI petrological classes were identified, *i.e.*, two-phase wüstite–olivine SI (Fig. 15a) and single-phase glassy SI (Fig. 15b). Example chemical data for the main mineralogical phases shown in Fig. 15 are reported in Table 2. It was found that the wüstite–olivine SI predominantly belong to forging-related groups 2(1) and 3(1). On the other hand, single-phase glassy SI having low iron oxide content are most prevalent in smelting-related groups 1(1) and 3. Moreover, it was observed that all SI located in the external martensitic zone of the blade sections S2 and S3 belong to the single-phase glassy type. On the other hand, no clear pattern has been found for SI in the inner portion of the blade. In fact, single-phase glassy and two-phase wüstite–olivine SI are spread in both ferritic–pearlitic (F+P) zones and in the blade core layer which is characterized by nodular pearlitic colonies and ferritic traces in a martensitic matrix (P*+M+F).

Analysis of the Steel Technological Origin

To assess the technological origin of the blade steel in terms of direct and indirect processes, the logistic regression method suggested by Disser et al. [29] was adopted. The data-driven model was built and tested starting from a learning set of samples with known technological origin [29]. It is worth noting that this statistical approach was applied in the present study under the assumption that the learning set includes samples that are representative of the unknown ironmaking process used to produce the sword blade steel. Given the chemical composition of smelting-related SI, this statistical model quantifies the probability of a binary variable (Y), classifying the process as direct (Y = 0) or indirect (Y = 1).

The model requires to transform the average weight oxides percentages of smelting-related SI (Oxide*) into subcompositional ratios (Oxide**) using Formula (3):

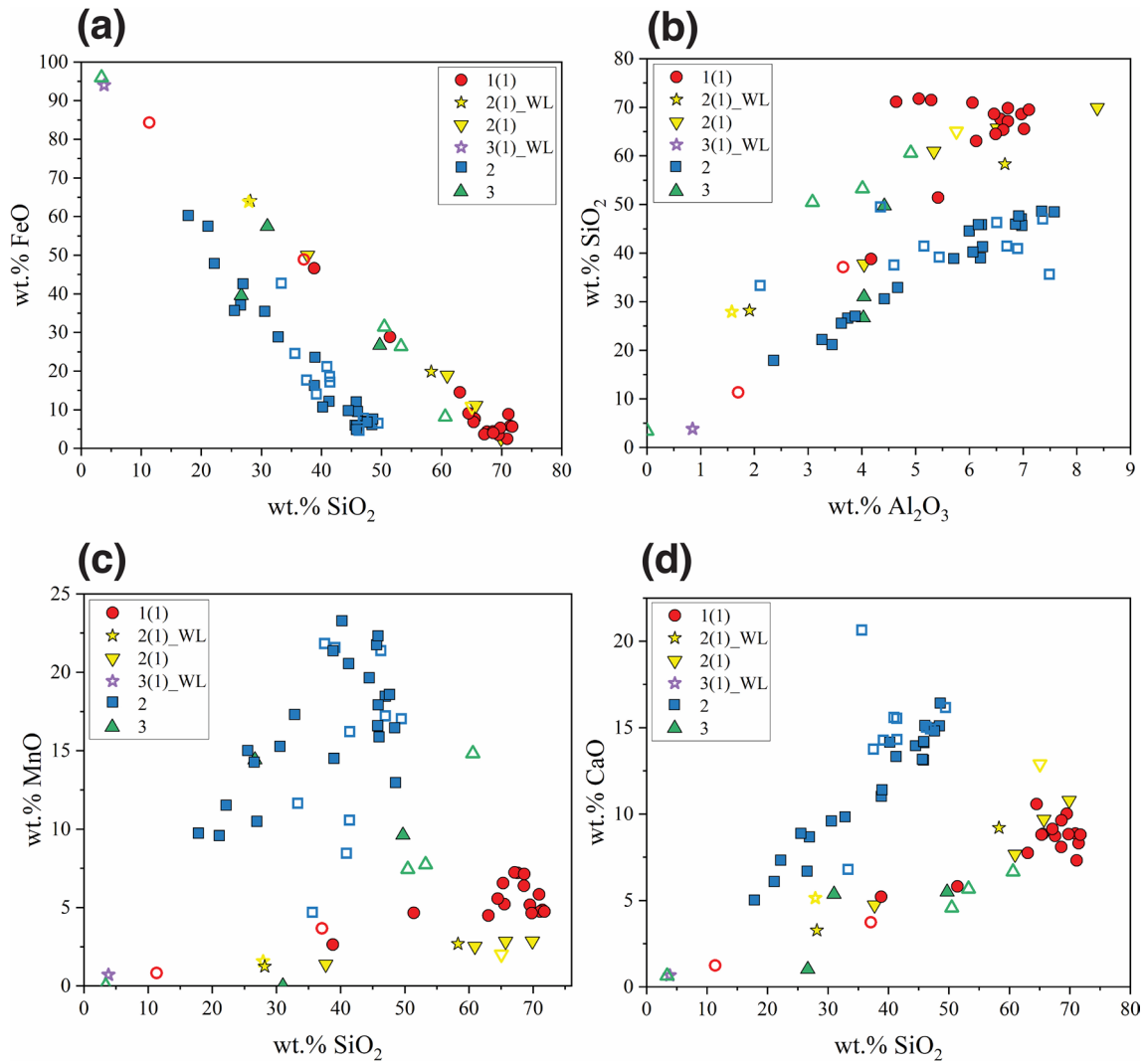$$\text{wt.\% Oxide}^{**} = (\text{wt.\% Oxide}^{*} \times 100)/(100 - \text{wt.\% FeO }*)$$

$$(3)$$

Fig. 14 Bivariate scatterplots: (**a**) FeO–SiO$_2$, (**b**) SiO$_2$–Al$_2$O$_3$, (**c**) MnO–SiO$_2$, and (**d**) CaO–SiO$_2$ (solid and open versions of the same symbol refer to S2 and S3 section, respectively; WL = white line)

Fig. 15 SEM micrographs of the two main SI mineralogical types: (**a**) two-phase wüstite (grey)–olivine (dark grey) SI, (**b**) single-phase glassy SI; Wus: wüstite, Ol: olivine, Gl: glass (abbreviations after Whitney and Evans [35]). The letters A, B, and C indicate the zones chemically analyzed by SEM/EDS
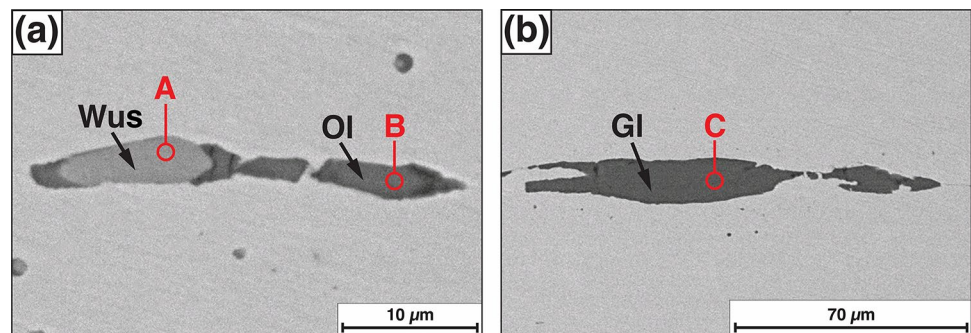
Table 2 SEM/EDS Microchemical analyses of the areas highlighted in Fig. 12

	MgO (wt.%)	Al$_2$O$_3$ (wt.%)	SiO$_2$ (wt.%)	K$_2$O (wt.%)	CaO (wt.%)	TiO$_2$ (wt.%)	MnO (wt.%)	FeO (wt.%)
A (wüstite)	0.00	0.00	0.00	0.00	0.00	0.00	0.94	99.06
B (olivine)	0.00	1.58	27.91	0.00	5.13	0.00	1.57	63.81
C (glass)	3.36	7.37	46.98	1.81	14.93	0.51	17.22	7.82

Table 3 Logistic regression model parameters

	Parameter	Value
Intercept	β^0	5.22
MgO	β^{Mg}	0.13
Al$_2$O$_3$	β^{Al}	−0.95
SiO$_2$	β^{Si}	0.007
P$_2$O$_5$	β^{P}	0.16
K$_2$O	β^{K}	−0.84
CaO	β^{Ca}	0.088
MnO	β^{Mn}	0.018

where "Oxide" indicates each oxide involved in the statistical analysis (*i.e.*, MgO, Al$_2$O$_3$, SiO$_2$, P$_2$O$_5$, K$_2$O, CaO, MnO). The logistic model can be expressed with Formula (4):

$$
\begin{aligned}
\text{Logit}(p) = \log\left[p/(1-p)\right] = {} & \beta^0 + \beta^{Mg}\left[\text{wt.\% MgO}^{**}\right] + \beta^{Al}\left[\text{wt.\% Al}_2\text{O}_3^{**}\right] + \beta^{Si}\left[\text{wt.\% SiO}_2^{**}\right] \\
& + \beta^{P}\left[\text{wt.\% P}_2\text{O}_5^{**}\right] + \beta^{K}\left[\text{wt.\% K}_2\text{O}^{**}\right] + \beta^{Ca}\left[\text{wt.\% CaO}^{**}\right] + \beta^{Mn}\left[\text{wt.\% MnO}^{**}\right]
\end{aligned}
\tag{4}
$$

In Formula (4), p is the probability that the binary variable Y equals unity (i.e., indirect process). The parameters of logistic regression (β^0, β^{Mg}, β^{Al}, β^{Si}, β^{P}, β^{K}, β^{Ca}, β^{Mn}) are reported in Table 3.

If $p < 0.3$ or $p > 0.7$, it is possible to identify the ironmaking technology as direct or indirect, respectively, as per reference [29]. Otherwise, the pyrometallurgical method is deemed undetermined. In the present study, the smelting-related SI of groups 1(1) and 2 were considered. The calculated oxides subcompositional ratios for these two groups are presented in Table 4.

The model yielded p values of 0.32 for group 1(1) and 0.63 for group 2. Given that these outcomes lie within the 0.3–0.7 range, it is not possible to definitely attribute groups 1(1) and 2 to direct or indirect process. However, based on these results, groups 1(1) and 2 seem to be more

compatible with the direct and indirect ironmaking processes, respectively.

Estimation of Smelting and Forging Temperatures

The temperature reached during the smelting and smithing manufacturing stages was evaluated by Rhyolite–MELTS v.1.0.2 software [36, 37]. The smelting and forging temperatures were assessed by estimating the liquidus temperature of smelting and forging SI, respectively. To this aim, the average chemical compositions of smelting-related SI groups 1(1) and 2 and forging-related SI group 2(1) were considered (Table 1). The thermodynamic modeling of liquidus temperatures was performed assuming a pressure of 1 bar (0.1 MPa) and iron–wüstite (IW) oxygen fugacity buffer (input files are provided in Electronic Supplementary Material). The results for smelting-related groups 1(1) and 2 are 1156°C and 1031°C, respectively. On the other hand, it was computed a liquidus temperature of 1143°C for the forging-related group 2(1). These values can be considered reasonable estimations of the lower limits of the maximum temperatures reached during the smelting and forging processes.

Conclusions

This archeometallurgical investigation was focused on a fragment of a medieval sword blade. Technological information about the manufacturing process employed to produce the sword blade was extracted from the object through a methodology based on metallography, Vickers microhardness tests, and slag inclusions analysis. Observations of the blade's microstructure, along with Vickers microhardness

Table 4 Oxides Subcompositional Ratios for Smelting-Derived SI of group 1(1) and 3

Group	MgO** (wt.%)	Al$_2$O$_3$** (wt.%)	SiO$_2$** (wt.%)	K$_2$O** (wt.%)	CaO** (wt.%)	MnO** (wt.%)	P$_2$O$_5$** (wt.%)
1(1)	2.49	6.87	72.47	1.46	9.31	6.09	0.00
2	3.93	6.91	47.97	1.29	14.99	22.18	2.28

measurements, unveiled an intricate forging process involving the meticulous assembly of diverse steel bars through hammer-welding techniques.

This process was aimed at achieving a delicate equilibrium between the hardness of the cutting edges and the overall toughness of the blade.

Notably, a steeling technique was applied by wrapping a steel bar around a composite steel billet which, in turn, was produced enveloping a hypoeutectoid steel bar around a near eutectoid steel core. Following the forging phase, the blade underwent heat treatment via quenching, giving rise to a martensitic microstructure at the outer steel layer that includes the cutting edges. An extensive dataset of slag inclusions (SI) compositional data was amassed through SEM/EDS analysis. The analysis of this dataset by multivariate statistics (PCA/HCA) and nonreduced compounds (NRCs) bivariate plots confirmed the composite nature of the blade and allowed to distinguish smelting and forging-related SI groups.

Specifically, it was found that the external portion and the blade core were made of steel produced in different technological systems. Moreover, the analysis of smelting-related SI groups by a classification model based on logistic regression indicated that the outer and inner portions of the sword blade were made of steel that possibly derived from the direct and indirect ironmaking processes, respectively. Finally, the lower limits of the maximum temperatures reached during both the smelting and forging phases were estimated by computing the liquidus temperatures of smelting and forging-derived SI using the Rhyolite–MELTS software. The analysis revealed that the smelting processes for the steel used in the external and internal parts of the blade reached temperatures of at least 1156°C and 1031°C, respectively. On the other hand, the peak forging temperature was determined to be at least 1143°C. These findings unveil the complex metallurgical history underlying the production of this medieval sword blade, enriching our understanding of ancient metallurgical techniques.

Declarations

Conflict of Interest The authors declare that they have no conflict of interest.

References

1. Oakeshott, E.: Records of the Medieval Sword, pp. 64–94. The Boydell Press: Woodbridge (1991).
2. C. Mapelli, W. Nicodemi, R.F. Riva, Microstructural investigation on a medieval sword produced in 12th century A.D. ISIJ Int. **47**, 1050–1057 (2007)
3. Pleiner, R.: Iron in archaeology: The European Bloomery Smelters, pp. 131–139. Archaeologicky Ustav Aver, Praha (2000).
4. Buchwald V.F.: Iron, Steel and Cast Iron before Bessemer: The Slag-Analytical Method and the Role of Carbon and Phosphorus. Historisk-filosofiske Skrifter 32, The Royal Danish Academy of Sciences and Letters, Copenhagen (2008).
5. J. Stelzner, F. Gauß, P. Schuetz, X-ray computed tomography for nondestructive analysis of early Medieval swords. Stud. Conserv. **61**, 86–101 (2016)
6. A. Williams, *The Sword and the Crucible: A History of the Metallurgy of European Swords up to the 16th Century* (Brill, 2012)
7. A. Williams, A metallurgical study of some viking swords. Gladius. **29**, 121–184 (2009)
8. A. Thiele, J. Hošek, P. Kucypera, L. Dévényi, The role of pattern-welding in historical swords-mechanical testing of materials used in their manufacture. Archaeometry. **57**, 720–739 (2016)
9. B. Gilmour, The metallurgy, development, and purpose of pattern welding. Hist. Metall. **51**, 57–70 (2017)
10. U. Lehmann, S. Roth, C. Lipka, Phosphoric Iron and Welded Patterns: The Reconstruction of an Early Medieval Sword from Beckumin, in *The Sword: Form and Thought*. ed. by L. Deutscher, M. Kaiser, S. Wetzler (The Boydell Press, Woodbridge, 2019), pp.43–60
11. H. Maryon, Pattern-welding and damascening of sword-blades: part 1 pattern-welding. Stud. Conserv. **5**, 25–37 (1960)
12. Pleiner R.: Iron in Archaeology: Early European Blacksmiths, pp. 200–212. Archaeologicky Ustav Aver, Praha (2006).
13. A. Williams, *The Knight and the Blast Furnace: A History of the Metallurgy of Armour in the Middle Ages and the Early Modern Period* (Brill, Boston, 2002), p.12
14. Buchwald V.F.: Iron and Steel in Ancient Times, pp. 274–282. Historisk-filosophiske Skrifter, Copenhagen (2005).
15. Samuels L.E.: Light Microscopy of Carbon Steels, pp. 312–15. ASM International, Materials Park, OH, (1999).
16. P. Merico, M. Faccoli, V. Ferrari, A. Breda, G. Cornacchia, Metallurgical and technological characterization of a lombard seax from North Italy. Metallogr. Microstruct. Anal. **10**, 1–18 (2021)
17. P. Merico, M. Faccoli, R. Gotti, G. Cornacchia, Archeometallurgical study of a renaissance spearhead from Northern Italy. Metall. Mater. Trans. B. **54**(1), 82–100 (2023)
18. P. Merico, M. Faccoli, R. Gotti, G. Cornacchia, Analysis of ancient slag inclusion-metal systems as a method to disclose processing thermo-chemical parameters: the case study of a medieval lombard steel bar from Northern Italy. Metall. Mater. Trans. B. **54**(3), 1408–1421 (2023)
19. G. Cornacchia, M. Faccoli, R. Roberti, Metallurgical Investigation of a Steel Miner's Chisel from Ponte Val Gabbia III Site. JOM. **67**, 260–271 (2015)

20. G. Cornacchia, R. Roberti, M. Faccoli, Characterization and technological origin identification of ancient iron nails. JOM. **72**, 3224–3235 (2020)
21. Tonelli G., Faccoli M., Gotti R., Roberti R., Cornacchia G.: Historical and Metallurgical Characterization of a "Falchion" Sword Manufactured in Caino (Brescia, Italy) in the Early 17th Century A.D.. JOM 68, 2233–2249 (2016).
22. P. Dillmann, M. L'Héritier, Slag inclusion analyses for studying ferrous alloys employed in French medieval buildings: supply of materials and diffusion of smelting processes. J. Archaeol. Sci. **34**, 1810–1823 (2007)
23. V.F. Buchwald, H. Wivel, Slag analysis as a method for the characterization and provenancing of ancient iron objects. Mater Charact. **40**, 73–96 (1998)
24. E. Bérard, P. Dillmann, O. Renaudeau, C. Verna, V. Toureille, Fabrication of a suit of armour at the end of middle ages: an extensive archaeometallurgical characterization of the armour of laval. J. Cult. Herit. **53**, 88–99 (2022)
25. E. Bérard, P. Dillmann, A. Disser, E. Vega, C. Verna, V. Toureille, The medieval bombards of Meaux: Manufacturing processes and supply of the metal. J. Archaeol. Sci. Rep. **41**, 103307 (2022)
26. Oakeshott R.E.: The Sword in the Age of Chivalry, pp. 37–41. Boydell Press, Woodbridge (1997).
27. C.A. Schneider, W.S. Rasband, K.W. Eliceiri, NIH Image to ImageJ: 25 years of image analysis. Nat. Methods. **9**, 671–675 (2012)
28. M. L'Héritier, A. Azéma, D. Syvilay, E. Delqué-Kolic, L. Beck, I. Guillot, M. Bernard, P. Dillmann, Notre-Dame de Paris: The first iron lady? Archaeometallurgical study and dating of the Parisian cathedral iron reinforcements. PLoS ONE. **18**, e0280945 (2023)
29. A. Disser, P. Dillmann, C. Bourgain, M. L'Héritier, E. Vega, S. Bauvais, M. Leroy, Iron reinforcements in Beauvais and Metz Cathedrals from bloomery or finery? The use of logistic regression for differentiating smelting processes. J. Archaeol. Sci. **42**, 315–333 (2014)
30. M.F. Charlton, E. Blakelock, M. Martinón-Torres, T. Young, Investigating the production provenance of iron artifacts with multivariate methods. J. Archaeol. Sci. **39**, 2280–2293 (2012)
31. J. Aitchison, The statistical analysis of compositional data. J. R. Stat. Soc. Ser. B. **44**, 139–177 (1982)
32. R Core Team: A Language and Environment for Statistical Computing, https://www.r-project.org/ (2020).
33. R.F. Tylecote, R. Thomsen, The segregation and surface-enrichment of arsenic and phosphorus in early iron artefacts. Archaeometry. **15**, 193–198 (1973)
34. R.F. Tylecote, Oxidation enrichment bands in wrought iron. Hist. Metall. **24**, 33–38 (1990)
35. D.L. Whitney, B.W. Evans, Abbreviations for names of rock-forming minerals. Am. Miner. **95**, 185–187 (2010)
36. M.S. Ghiorso, G.A.R. Gualda, MELTS_Excel: A Microsoft Excel-based MELTS interface for research and teaching of magma properties and evolution. Contrib. Miner. Petrol. **169**, 1–30 (2015)
37. G.A.R. Gualda, M.S. Ghiorso, R. Lemons, T.L. Carley, Rhyolite-MELTS: A modified calibration of MELTS optimized for silica-rich. Fluid-bearing Magmat. Systems. J. Petrol. **53**, 875–890 (2012)